Journal of Computational Applied Mechanics 2025, 56(1): 145-161

DOI: 10.22059/jcamech.2024.377299.1113

RESEARCH PAPER

Comparative Investigation of Deflection in a Two-directional Functionally Graded Porous Curved and Straight Beams Adapting Unified Shear Deformation Theory

G. Chandra Mohana Reddy [a, *], Valiveti Sivarama Krishna [b], Shaik Hussain [c], P. Bridjesh [d]

[a] *Department of Mechanical Engineering, MLR Institute of Technology, Hyderabad, India*
[b] *Department of Mechanical Engineering, VNRVJIET, Hyderabad, India*
[c] *Department of Mechanical Engineering, Malla Reddy Engineering College, Hyderabad, India*
[d] *Department of Chemical & Materials Engineering, College of Science, Engineering and Technology, University of South Africa (UNISA), c/o Christiaan de Wet & Pioneer Avenue, Florida Campus 1710, Johannesburg, South Africa*

Abstract

Functionally graded (FG) materials exhibit spatial variations in composition and structure, which enhance their performance under mechanical loads by tailoring material properties such as modulus of elasticity and density along the beam's length or thickness. This study presents a comparative analysis of the deflection behaviors of two-directional functionally graded porous beam, specifically focusing on circular and straight beams. Curved and straight beams are modeled and assessed under simply supported (SS), clamped (CC) and clamped simply supported (CS) boundary conditions with a mechanical load. The analysis involves deriving deflection equations considering the graded material properties, which vary according to a power-law distribution, adapting unified shear deformation theory (USDT), potential energy, neutral surface concept for better accuracy.

Keywords: Circular beam; Bending characteristic; Shear function; Porosity; Neutral surface.

1. Introduction

Functionally graded materials offer numerous benefits like enhanced stress distribution, high temperature tolerance, and strength, making them useful in various technical fields like aerospace, automotive, electrical, construction, and biomedical. Used shear deformation theories, namely two- and quasi-three-dimensional ones, are utilized to examine the behavior of FG, simply supported beams under various circumstances, including vibration, buckling, and bending. In a situation with a simply supported beam and an evenly distributed load [1]. Established exact analytical solutions. Third-order shear deformation was used to formulate specific analytical formulas, which were then compared to both the conventional analytical formula and the currently available numerical data [2]. Using a broad third order plate theory, analyzed the behavior of FG porous microplates under static bending, free vibration, and buckling. The analytical solutions were obtained by applying Navier's approach [3]. Higher order theory analysis examined bending behavior of FG curved beams in elevation, considering shear deformation and thickness stretching effects, and examining sandwich beams with symmetric and asymmetric cores [4]. Employed classical and first order

* Corresponding author. Tel.: +91-8297909752; *E-mail address:* cmreddy115@gmail.com

shear deformation plate theories to examine the buckling, vibration, and bending behaviors of FG porous micro-plates. The Navier solution approach and power-law distribution were implemented for analysis [5].

Adapted a global-local shear deformation theory for the behavior of thin and thick layered curved beams, considering deepness and a locally refined shear stress function [6]. Aimed to develop a computational approach for designing and optimizing device components in micro- and nano-electromechanical systems by combining modified couple stress theory with isogeometric analysis framework [7]. Introduced a layer wise approach for analyzing static, free, and forced vibrations of circular curved beams with significant curvature, using Hamiltonian technique for consistent dynamics and stress results [8]. Introduced an improved shear deformation beam theory for analyzing bending characteristics of functionally graded sandwich curved beams, providing a parabolic variation in shear stress distribution along thickness direction, eliminating shear correction components [9]. Explored the static behavior of FG sandwich curved beams using sinusoidal beam theory, considering transverse normal stress/strain. The beam consists of functionally graded skins and an isotropic core. Material qualities are distributed throughout thickness [10].

The study examines the flexural characteristics of two-directional functionally graded beams (FGBs) under different boundary circumstances. This investigation utilizes a shear and normal deformation theory in conjunction with the Symmetric Smoothed Particle Hydrodynamics (SSPH) approach [11]. Analyzed free vibration of curved sandwich beams in elevation using a fifth-order curved beam theory, considering transverse shear and normal strains, and solving equations of motion using Navier's technique [12]. Discussed Navier's solution for curved beams with simple support, but the case is mathematically indeterminate. Timoshenko theory is used for governing differential equations [13]. Investigated the bending and inherent vibration of porous functionally graded (PFG) beams that are upheld by elastic foundations, with a specific emphasis on the diverse material characteristics and the medium of the foundation [14]. Analyzed the thermal buckling problem in porous thick rectangular plates composed of FGM using a high-order shear theory. The investigation took into account material characteristics such as Young's modulus and the variation of thermal expansion in the thickness direction [15]. Explored the natural frequencies of P/IP-FGSBs, consisting of a porous core made of FGMs and homogenous isotropic metal and ceramic face sheets supported by elastic foundations [16]. Explored the influence of porosity distribution patterns on free vibration analysis in porous FG plates under different boundary conditions, considering continuous material properties and porosities based on volume fraction [17]. Explored the elastic limit of functionally graded porous rotating disks using a method that models their mechanical characteristics using four porosity models and Galerkin's error minimization theory [18]. Examined the static deformation and free vibration of porous circular beams, considering both even and uneven porosities. The study uses the Navier type closed-form solutions, derived from the higher-order hyperbolic circular beam theory, to address transverse shear deformation and rotating inertia [19]. Studied functionally graded materials (FGMs) to enhance sandwich beam endurance, but technical issues may cause pores. This study examines porosity's impact on fundamental natural frequencies of FG sandwich beams using advanced beam theory [20].

Introduced an extension of QEM to study free vibration of 3D parallelepipeds made of multi-directional functionally graded material, providing formulations for continuous variations in material characteristics [21]. Presented a numerical investigation of post buckling behavior of multi-directional Functionally Graded Material (FGM) plates, combining NURBS-based IGA with FCM for the first time [22]. Introduced a computational method for analyzing bending and free vibration characteristics of functionally-graded plates in three dimensions, considering heat conditions and using generalized heat transfer equations [23]. Examined free vibration on a sandwich plate with multi-directional porous functionally graded material, using Hamilton's concept and Navier's approach. The plate was examined under two conditions, avoiding surface traction and using shear correction coefficients [24]. Examined the bending and buckling of a multi-directional porous sandwich plate, considering two cases with functionally graded skin and homogeneous core, using Navier's approach to achieve a solution without shear correction factors [25].

Examined the hygro-thermal vibration of curved BDFGP beams supported by two-layer elastic foundations. Using GFEM, it analyzed the dynamic behavior of Winkler springs and shear springs, creating an enriched mathematical space [26]. Investigated the natural oscillation of a 2D-FG curved nanobeam, functionally graded in two directions, using Hamilton's principle and FSDT. The nonlocal elasticity hypothesis of Eringen’s accounts for the small-scale effect [27]. Explored the free vibrations of curved zigzag nanobeams using sinusoidal beam theory and doublet mechanics formulation, developing a finite element doublet mechanics model and comparing results [28]. Earlier research has examined the structural analysis of functionally graded beams and their mechanical properties, but a thorough comparison analysis that specifically investigates the deflection behavior under different boundary conditions utilizing advanced modeling approaches has not been extensively investigated. The Mori-Tanaka model is used to analyze earthquake loads on concrete pipes with SiO2 nanoparticles and fiber reinforced polymer layer, using cylindrical higher order shell theory for governing relations [29]. This study analyzes the mechanical properties of 7075-T6 aluminum reinforced with SiC particles using vortex casting method and standard tensile test specimens fabricated using CNC machining [30].

The paper proposes a novel hybrid optimization method based on particle swarm optimization and harmony search

algorithms to optimize the dynamic properties of a laminated sandwich multiphase nanocomposite truncated conical shell under magneto-hygro-thermal conditions [31]. The article investigates the supersonic flutter behavior and reliability of smart hybrid nanocomposite trapezoidal plates in aerospace engineering, using the Halpin-Tsai model and actuators and sensors [32]. The study examines the influence of moving loads and piezoelectric patches on energy harvesting and dynamic behavior of a nano conical panel made from SMA [33]. The article investigates wave propagation in micro air vehicle wings using mathematical modeling, incorporating porous FGM and magneto strictive nanocomposite layers for enhanced stiffness and control [34]. This study presents a numerical benchmark for hydrodynamic analysis and smart control of wave-piercing catamaran beam elements using a 2D Wanger type impact force model, proportional-differential controller, and energy technique [35]. The paper explores wave propagation in micro-sandwich beams made of auxetic honeycomb, piezoelectric, and Two-Dimensional Functionally Graded Material, analyzing wave velocity, escaping frequency, and cut-off frequency [36]. The study investigates the dynamic stability response of a micro sandwich beam with a rheological elastomer core, utilizing viscoelastic models and theories [37]. The study examines energy absorption in a conical three-layered panel with piezoelectric upper, graphene nanoplatelets, auxetic core, and porous lower layer using Hamilton's principle, energy method, and differential Cubature method [38]. The study examines the effects of reinforcing a hybrid nanocomposite viscoelastic rhombic plate with carbon nanotubes and carbon fibers on vibrations, energy absorption, and post-buckling behavior [39].

Exploring FG materials in both curved and straight geometries present opportunities for novel applications. Curved beams are commonly seen in the fields of aerospace, automotive, and civil engineering. By comparing these materials with typical straight beams, a more comprehensive understanding of the optimal utilization of FG materials in different sectors can be achieved. The study offers valuable insights into optimizing beam design for specific mechanical loads and boundary conditions by comparing the deflection behaviors of curved and straight FG porous beams. Implementing this optimization can result in structural designs that are more efficient and cost-effective, leading to reduced material wastage and enhanced load-bearing capacities.

This study explores the use of Kuhn-Tucker conditions in solving the governing equations in the bending analysis in FG porous structures, aiming to improve existing methods and explore the correlation between material classification and porosity distribution, potentially revealing unique phenomena. This study examines the flexural characteristics of a two-directional functionally graded curved porous beam (2DFGPCB) adapting unified shear deformation theory and a comparison will be made between the structural analysis of curved and straight beams under simply supported (SS), clamped (CC) and clamped simply supported (CS) boundary conditions. These approaches improve the precision of deflection predictions and aid in the advancement of increasingly complex analytical models.

2. Mathematical formulation

Accordance with HSDT, beam is conceptualized as a slender structural component that exhibits shear and bending properties. The beam is considered to have a curved shape and uniform properties throughout its length, exhibiting minor distortions and governed by linear equations. Warping effects, which involve the twisting of the cross-section, are not taken into account. Instead, it is assumed that the cross-sections, which were initially flat, remain flat following deformation. The assumption is made that the material properties remain consistent along the entire length of the beam, which allows for easier computations and analytical solutions. The current study used the coordinate system depicted in Fig 1. for 2DFGPCB. Both length and thickness dimensions exhibit continuous variation in the material properties. The thickness-dependent variation of ceramic and metallic phases symbolizes the FG curved beam. At $z = -h/2$, the lower section of the beam is constructed of metal, whereas at $z = +h/2$, the upper segment is composed of ceramic.

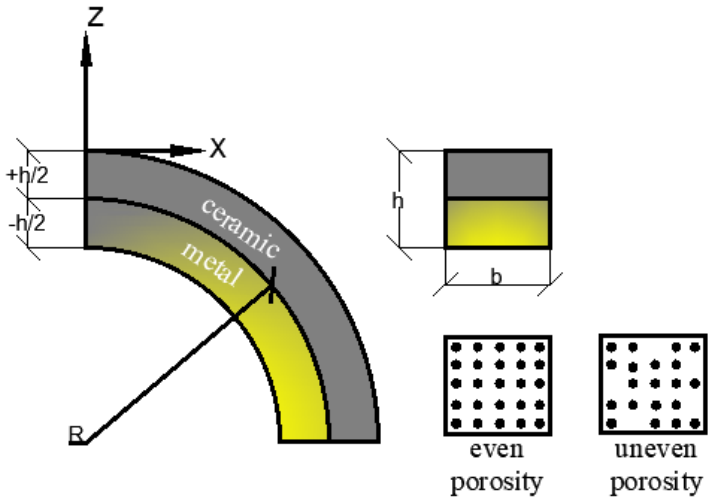

Fig 1: beam characterized by functional grading and varying porosity

2.1. Material homogenization

The fabrication of FG beams is influenced by the volumetric composition of the constituent materials. A functional and structural relationship between the thickness and properties of the material is to be anticipated. The power law distribution in *x* and *z*, represented as (V_{f1}), provides an accurate representation of the volume fraction of a single constituent, as illustrated in equation 1 [11] .

$$V_{f1}(x,z) = \left(\frac{z}{h}+\frac{1}{2}\right)^{P_z}\left(\frac{x}{L}+\frac{1}{2}\right)^{P_x} \quad (1)$$

$$V_{f1}(x,z) + V_{f2}(x,z) = 1 \quad (2)$$

Within particular framework, the gradient indices P_x and P_z denote volume fraction's behavior along entire length and thickness the beam, respectively. The functional properties of material, $P(x,z)$ consisting uniformly distributed 2DFGPCB can therefore be represented as,

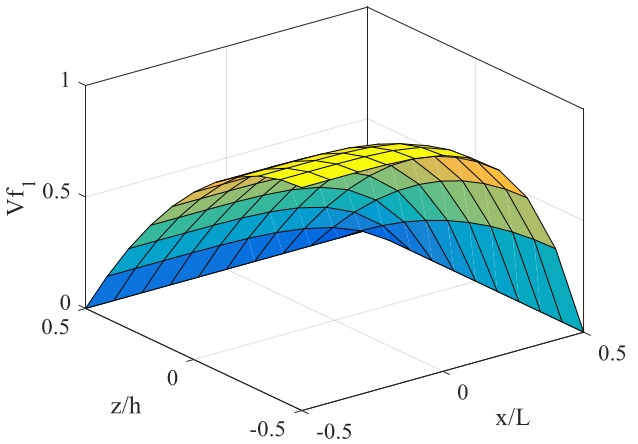

Fig 2: Metal volume fractions in the direction of length (x/L) and thickness (z/h).

$$P(x,z) = (P_c - P_m)\left(\frac{z}{h}+\frac{1}{2}\right)^{P_z}\left(\frac{x}{L}+\frac{1}{2}\right)^{P_x} + P_m - \frac{\alpha}{2}(P_c + P_m) \quad (3)$$

Symbol 'α' represents the porosity coefficient, which is a value between 0 to 1. The variable '*m'* indicates presence of metal, while '*c'* indicates presence of ceramic. According to previously indicated connection, Modulus of Elasticity $E(x,z)$ is used to evaluate material rigidity and moment of inertia in an evenly distributed 2DFGPCB, and it may be mathematically represented as shown in equation (4).

$$E(x,z) = (E_c - E_m)\left(\frac{x}{L}+\frac{1}{2}\right)^{P_x}\left(\frac{z}{h}+\frac{1}{2}\right)^{P_z} + E_m - \frac{\alpha}{2}(E_c + E_m) \quad (4)$$

Little difference when utilizing Poisson's ratio in compared to other attributes, considered unaffected because computations are performed using the mean value. Similarly, equation (5) can be used to derive the impact

characteristics of a distributed but even 2DFGPCB component.

$$P(x,z) = (P_c - P_m)\left(\frac{z}{h}+\frac{1}{2}\right)^{P_z}\left(\frac{x}{L}+\frac{1}{2}\right)^{P_x} + P_m - \frac{\alpha}{2}(P_c + P_m)\left(1 - \frac{2|z|}{h}\right) \quad (5)$$

The young modulus (E) for irregularly distributed FGPCB can be approximated using equation (6).

$$E(x,z) = (E_c - E_m)\left(\frac{z}{h}+\frac{1}{2}\right)^{P_z}\left(\frac{x}{L}+\frac{1}{2}\right)^{P_x} + E_m - \frac{\alpha}{2}(E_c + E_m)\left(1 - \frac{2|z|}{h}\right) \quad (6)$$

Fig 3. illustrates the relationship between the dimensionless modulus of elasticity (E/E_c) and the dimensionless length (x/L) for the 2DFGPCB with different values of P_x. As the value of P_x increases, the modulus of elasticity decreases more sharply along the length of the beam. This indicates that higher values of P_x correspond to stronger gradations in material properties. The different curves emphasize the ability to intentionally develop functionally graded materials with precise property distributions. Decreasing the values of P_x leads to a more consistent distribution of material qualities, whilst increasing the values of P_x introduces more pronounced fluctuations, which can be customized for specific engineering purposes. Comprehending these curves aids in the creation of materials and structures with certain stiffness distributions, hence enhancing performance under mechanical stresses, increasing durability, and optimizing material utilization. Fig 4. illustrates the relationship between the dimensionless modulus of elasticity (E/E_c) and the dimensionless length (x/L) for the 2DFGPCB with different values of P_z. As the value of P_z increases, the modulus of elasticity increases more sharply along the thickness of the beam. This indicates that higher values of P_z correspond to stronger gradations in material properties. The varying curves highlight how functionally graded materials can be designed to have specific property distributions. Lower values of P_z result in more uniform material properties, while higher values create more significant variations, potentially tailored for specific engineering applications.

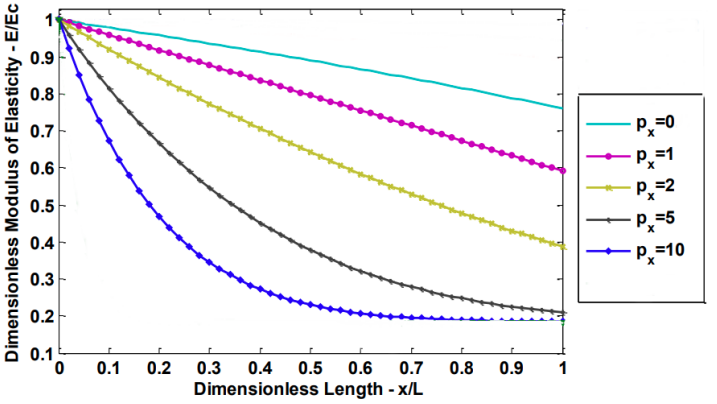

Fig 3: The effect of P_x on the dimensionless modulus of elasticity

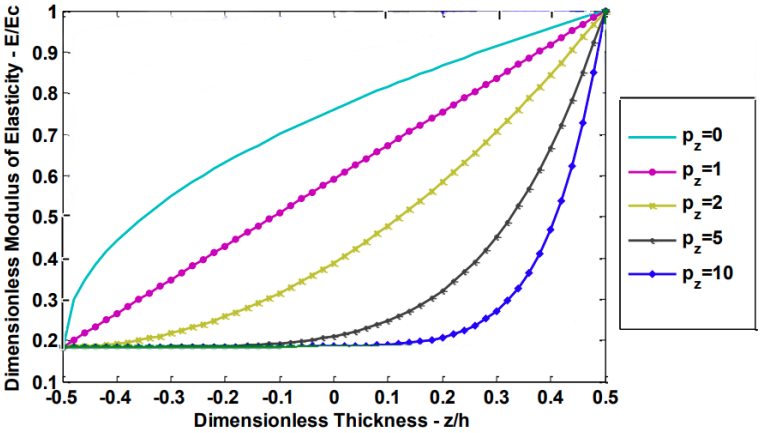

Fig 4: The effect of P_z on the dimensionless modulus of elasticity

FG plates and beams are crucial for static and dynamic structures, reducing manufacturing costs. Classic beam and plate theories often overestimate structural deflections, critical loads, and natural frequencies. Shear deformation FG beam theories enhance forecast precision. The 2DFGPCB cartesian coordinate system, thickness, and porosity impact deformations and displacements. Constitutive equations (7) and (8) determine the displacement field.

$$U(x,z) = \left(1+\frac{z}{R}\right)u_0(x,t) - z\frac{\partial w_0}{\partial x}(x,t) + f(z)\left(\emptyset(x,t) + \frac{\partial w_0}{\partial x}(x,t)\right) \quad (7)$$

$$W(x,z) = w_0(x,t) \tag{8}$$

Axial displacement is represented by $U(x,z)$, whereas transverse displacement is represented by $W(x,z)$. At each certain location on the neutral axis, $u_0(x,t)$ represents the axial displacement and $w_0(x,t)$ represents the transverse displacement. Bending slope is represented by the partial derivative $\frac{\partial w_0}{\partial x}(x,t)$, while $\emptyset(x,t)$ represents the shear slope. Use the shape function $f(z)$ to figure out the transverse shear displacement, and equations (7) and (8) can be used to find the mathematical equations that represent the non-zero stresses.

$$\varepsilon_x = \frac{\partial U}{\partial x} + \frac{W}{R} = \frac{\partial u_0}{\partial x} - z\frac{\partial^2 w_0}{\partial x^2} + f(z)\left(\frac{\partial \emptyset}{\partial x} + \frac{\partial^2 w_0}{\partial x^2}\right) + \frac{W_0}{R} \tag{9}$$

$$\varepsilon_z = \frac{\partial W}{\partial Z} = 0 \tag{10}$$

$$\gamma_{xz} = \frac{\partial U}{\partial z} + \frac{\partial w}{\partial x} - \frac{u_0}{R} \tag{11}$$

$$\gamma_{xz} = f'z\left[\emptyset + \frac{\partial w_0}{\partial x}\right] - \frac{u_0}{R} \tag{12}$$

$$f(z) = z\left[\frac{1}{h} - sin\frac{\pi}{3h}\right] \tag{13}$$

The function $f(z)$ is incorporated into the displacement field of higher order theories to consider the impact of transverse shear deformation and achieve zero shear stress conditions at the top and bottom surfaces of the beam. The term z suggests a linear variation with the position along the height of the beam. This implies that the shear deformation is proportional to the distance from the mid-plane (neutral axis) of the beam. The term $\frac{1}{h}$ normalizes the linear variation to account for the total thickness of the beam, ensuring the function scales appropriately with the beam's height. The sine term introduces a periodic variation within the linear profile. The specific form $sin\frac{\pi}{3h}$ means the sine function oscillates along the height of the beam, modulating the linear shear distribution. The combination $z\left[\frac{1}{h} - sin\frac{\pi}{3h}\right]$ results in a shear shape function that starts linearly but is adjusted periodically by the sine term. This reflects the actual physical behavior of shear deformation in beams, where the distribution of shear stress and strain is not purely linear due to the material's response to loading and boundary conditions. In structural analysis, particularly in advanced beam theories like USDT, shear shape functions are used to accurately model the distribution of shear stresses and strains within the beam's cross-section. The function $f(z)$ helps in capturing the non-linear shear effects that are significant in thick beams or beams made of functionally graded materials. Through the utilization of equations (9) and (11) in conjunction with Hooke's law, the subsequent field equations can be formulated to represent stress:

$$\sigma_x = E(x)\varepsilon_x \tag{14}$$

and $$\tau_{xz} = \frac{E(x)}{2(1+\mu)}\gamma_{xz} \tag{15}$$

2.2. Material homogenization

Hamilton's principle is a crucial topic in the field of bending analysis. The derivation of the essential equations of elasticity and dynamics is as described in reference [14].

$$B = \int_{t1}^{t2}(\delta U + \delta V)\,dt = 0 \tag{16}$$

t_1 and t_2 represent time intervals, δU and δV represent variations in the potential energy of the strain, as well as the amount of work performed. The shift in strain energy that happens in a 2DFGPCB can be characterized.

$$\delta U = \frac{1}{2}\int_0^L \int_{-\frac{h}{2}}^{+\frac{h}{2}}(\sigma_x\varepsilon_x + \tau_{xz}\gamma_{xz})dzdx \tag{17}$$

$$\delta V = -\int_0^L q\delta w_0\,dx \tag{18}$$

Substituting equations. (9), (11), (14), and (15) into Eq. (16), strain energy could be deduced as,

$$B = \int_0^L \int_{-\frac{h}{2}}^{+\frac{h}{2}}(\sigma_x\varepsilon_x + \tau_{xz}\gamma_{xz})dzdx - \int_0^L q\delta w_0\,dx \tag{19}$$

$$= \int_0^L \int_{-\frac{h}{2}}^{+\frac{h}{2}}\left(\sigma_x\left(\frac{\partial u_0}{\partial x} - z\frac{\partial^2 w_0}{\partial x^2} + f(z)\left(\frac{\partial \emptyset}{\partial x} + \frac{\partial^2 w_0}{\partial x^2}\right) + \frac{W_0}{R}\right) + \tau_{xz}\left(f'z\left[\emptyset + \frac{\partial w_0}{\partial x}\right] - \frac{u_0}{R}\right)\right)dzdx - \int_0^L q\delta w_0\,dx \tag{20}$$

$$= \int_0^L \int\left(\left(N_x\frac{\partial u_0}{\partial x} - M_x{}^b\frac{\partial^2 w_0}{\partial x^2} + M_x{}^s\left(\frac{\partial \emptyset}{\partial x} + \frac{\partial^2 w_0}{\partial x^2}\right) + \frac{W_0}{R}\right) + \left(Q_x\left[\emptyset + \frac{\partial w_0}{\partial x}\right] - \frac{u_0}{R}\right)\right)dzdx - \int_0^L q\delta w_0\,dx \tag{21}$$

where M_x and Q_x value for shear force and bending moment, respectively. P_x and R_x represent the resultants of higher order stresses.

$$N_x = \int_{-\frac{h}{2}}^{+\frac{h}{2}} \sigma_x dZ \tag{22}$$

$$M_x{}^b = \int_{-\frac{h}{2}}^{+\frac{h}{2}} \sigma_x \, z dZ \tag{23}$$

$$M_x{}^s = \int_{-\frac{h}{2}}^{+\frac{h}{2}} \sigma_x \, f(z) dZ \tag{24}$$

$$Q_x = \int_{-\frac{h}{2}}^{+\frac{h}{2}} \tau_{xz} \, f'(z) dZ \tag{25}$$

2.3. Kuhn Tucker Solution

If the function $f_0(x)$ achieves a local minimum at point x^0, subject to the set $K=x/(f_i(x)) \leq 0$ (where i=1, 2, 3, …. m), and f_k (x) (where k=0, 1, 2, ….. m) are all differentiable, then there exists a vector of Lagrange multiplier U^0 that satisfies the following conditions.

$$\frac{\partial f_0(x^0)}{\partial x_j} + \sum_{i=1}^{m} U_i^0 \, \frac{\partial f_0(x^0)}{\partial x_j} = 0 \;\; (j = 1, 2, 3, \ldots \ldots, n) \tag{26}$$

$$f_i(x^0) \leq 0 \; (i = 1, 2, 3, \ldots . m)$$

$$u_i^0 f_i(x^0) = 0 \; (i = 1, 2, 3, \ldots . , m)$$

$$u_i^0 \geq 0 \; (i = 1, 2, 3, \ldots . m)$$

The conditions that are essential for a local minimum in optimization problems are referred to as the Kuhn Tucker condition, while the non-negativity condition $U^0 \leq 0$ is crucial for maximization problems.

$$L(x, y, u) = f_0(x) + \sum_{i=1}^{m} u_i (f_i(x) + y_i^2) \tag{27}$$

The necessary condition for its local minimum is

$$\frac{\partial L}{\partial x_j} = \frac{\partial f_0(x^0)}{\partial x_j} + \sum_{i=1}^{m} u_i^0 \frac{\partial [f_i(x^0) + (y_i^0)^2]}{\partial x_j} = 0 \tag{28}$$

$$\frac{\partial L}{\partial y_i} = 2 u_i^0 y_i^0 = 0 \;\; (j = 1, 2, 3, \ldots . n)$$

$$\frac{\partial L}{\partial u_i} = f_i(x^0) + (y_i^0)^2 = 0 \;\; (i = 1, 2, 3, \ldots m)$$

$$\frac{\partial f_0[x^0(b)]}{\partial b_i} = -u_i^0 \;\; (i = 1, 2, 3, \ldots . m)$$

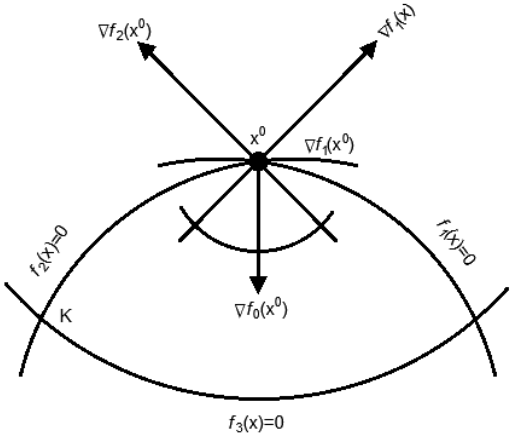

Fig 5: Kuhn Tucker condition

Without slack variables, the mathematical problem,

$$L(x,u) = f_0(x) + \sum_{i=1}^{m} u_i f_i(x) \tag{29}$$

The Kuhn Tucker condition can be rewritten as,

$$\frac{\partial L(x^0,u^0)}{\partial x_j} = 0 \quad (j = 1,2,3,\ldots..n)$$

$$\frac{\partial L(x^0,u^0)}{\partial u_i} \leq 0 \quad (i = 1,2,3,\ldots..m)$$

$$u_i^0 \ \frac{\partial L(x^0,u^0)}{\partial u_i} = 0 \quad (i = 1,2,3,\ldots..m)$$

$$u_i^0 \geq 0 \ (i = 1,2,3,\ldots m)$$

When u_i is positive, it indicates that the corresponding i^{th} constraint is binding, indicating a boundary solution. The function $u_0(x, y)$, $w_0(x, y)$, and $\cup_0(x, y)$ can be mathematically represented as Lagrange equations when they are expressed as generalized coordinates. The Kuhn Tucker condition, specified by the table values, can be expressed as follows.

$$u_0(x,y) = \sum_{i=1}^{m} f_i(x^0)\theta_i e^{i\lambda y} \tag{30}$$

$$w_0(x,y) = \sum_{i=1}^{m} f_i(x^0)\varphi_i e^{i\lambda y} \tag{31}$$

$$\emptyset_0(x,y) = \sum_{i=1}^{m} f_i(x^0)\psi_i e^{i\lambda y} \tag{32}$$

where, θ_i, φ_i, and ψ_i are the three different boundary conditions and λ is the scalar. Kuhn Tucker boundary conditions are utilized for mathematical calculations as stated in Table 1.

$$\begin{bmatrix} K_{11} & K_{12} & K_{13} \\ K_{21} & K_{22} & K_{23} \\ K_{31} & K_{32} & K_{33} \end{bmatrix} \begin{bmatrix} u_0 \\ w_0 \\ \emptyset_0 \end{bmatrix} = \begin{bmatrix} 0 \\ q \\ 0 \end{bmatrix} \tag{33}$$

$$K_{11}(i,j) = \frac{E(x,z)}{1-\mu^2}\int_0^L e^{\lambda x(x+1)}\,\theta_{i,x},\theta_{j,x}dx \tag{34}$$

$$K_{12}(i,j) = \frac{E(x,z)}{1-\mu^2}\int_0^L e^{\lambda x(x+1)}\,\theta_{i,x},\varphi_{j,x}dx \tag{35}$$

$$K_{13}(i,j) = \frac{E(x,z)}{1-\mu^2}\int_0^L e^{\lambda (x+1)}\,\theta_{i,x},\psi_{i,x}dx \tag{36}$$

$$K_{22}(i,j) = \frac{E(x,z)}{1-\mu^2}\int_0^L e^{\lambda x(x+1)}\,\varphi_{i,xx},\varphi_{j,xx}dx \tag{37}$$

$$K_{23}(i,j) = \frac{E(x,z)}{1-\mu^2}\int_0^L e^{\lambda x(x+1)}\,\varphi_{i,xx},\psi_{j,xx}dx \tag{38}$$

$$K_{33}(i,j) = \frac{E(x,z)}{1-\mu^2}\int_0^L e^{\lambda x(x+1)}\,\psi_{i,xx}\psi_{j,xx}dx \tag{39}$$

where, $i,j = 1,2,3,\ldots\ldots n$

3. Result and discussion

The numerical investigations based on USDT are carried out to predict the static analysis of 2DFGPCB with various conditions at the boundary like SS and CC as shown in Table 1. Numerical findings are derived based on Navier's solutions. The 2DFGPCB consists of Aluminum metal with a modulus of elasticity (E_m) of 70 GPa, a Poisson's ratio (μ_m) of 0.3, and a density (ρ_m) of 2702 kg/m^3. It also includes Alumina ceramic with a youthful modulus (E_c) of 380 GPa, a Poisson's ratio (μ_c) of 0.3, and a density (ρ_c) of 3960 kg/m^3. According to the power-law distribution, the properties of 2DFGPCB are changing in both the thickness and length directions.

Table 1: Boundary conditions based on the Kuhn Tucker solution

Boundary Condition	x = 0	x = L
SS	u = 0, w = 0	w = 0
CC	u = 0, w = 0, ∅=0, w′ = 0	u = 0, w = 0, ∅=0, w′ = 0
CS	u = 0, ∅ = 0, w = 0, w′ = 0	u = 0, w = 0

For representation of results, following dimensionless forms are used.

Transverse displacement (w)

$$\overline{w} = \frac{w100E_m h^3}{q_0 L^4} \tag{40}$$

Table 2: Evaluation of dimensionless transverse deflection values of SS 2DFGPCB using different theories at different aspect ratios (L/h = 5, L/h = 20) and gradation exponents.

Method	Theory	ε_z	P = 0	P = 1	P = 2	P = 5	P = 10
			L/h = 5, R/L = 5				
[11]	SNDT	= 0	3.1397	6.1338	7.8606	9.6037	10.8979
present	USDT	= 0	3.2966	6.4457	8.2536	10.0838	11.4428
			L/h = 20, R/L = 5				
[11]	SNDT	= 0	2.8947	5.7201	7.2805	8.6479	9.5749
present	USDT	= 0	3.0394	6.0061	7.6445	9.0802	10.0536

Table 3: The dimensionless transverse deflection values of a SS 2DFGPCB with both even and uneven porosity, an aspect ratio of L/h = 5, and gradation exponents are being considered.

P_x & P_z	L/h = 5	even porosity			P_x & P_z	L/h = 5	uneven porosity		
	0	0.1	0.2	0.3		0	0.1	0.2	0.3
0	3.2966	3.5131	3.7029	4.0464	0	3.2966	3.4297	3.5967	3.6667
1	7.38280	7.9595	8.6353	9.4364	1	7.3828	7.5318	7.6880	7.8513
2	10.0844	10.8721	11.7952	12.8894	2	10.0844	10.2879	10.5013	10.7243
5	13.6706	14.7384	15.9899	17.4732	5	13.6706	13.9465	14.2358	14.5381
10	16.0113	17.2620	18.7277	20.4650	10	16.0113	16.3344	16.6733	17.0273

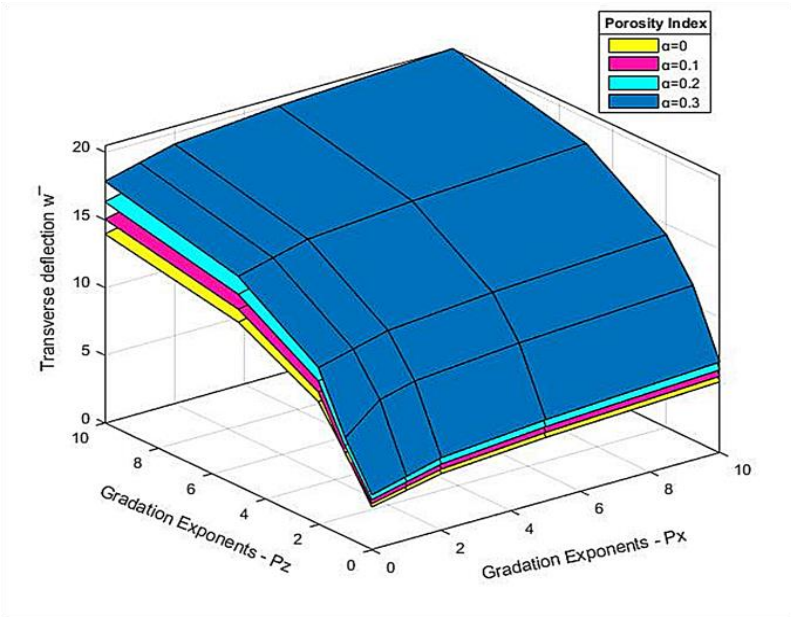

(a)

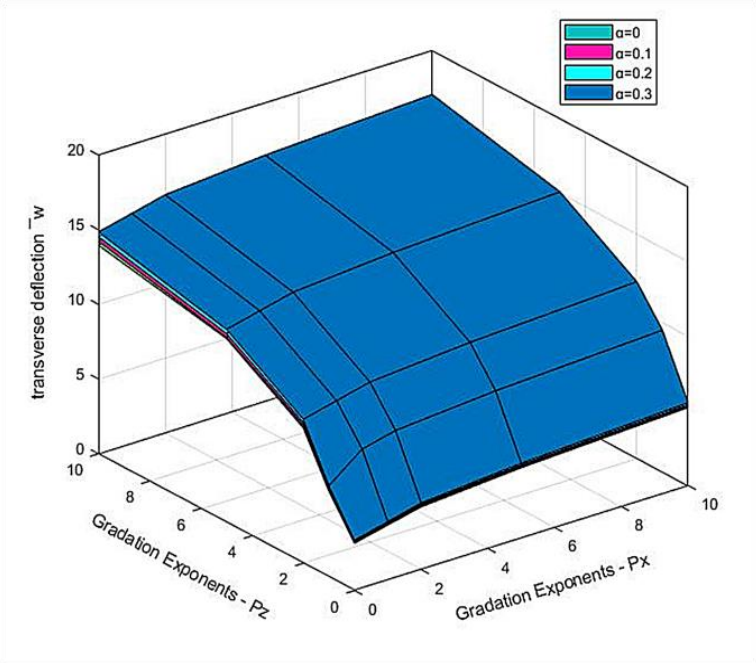

(b)

Fig 6: The dimensionless transverse deflection values of a SS 2DFGPCB with (a) even and (b) uneven porosity, an aspect ratio of L/h = 5, and gradation exponents.

Table 4: Evaluation of dimensionless transverse deflection values of CC 2DFGPCB using different theories for different aspect ratios (L/h = 5, L/h = 20) and gradation exponents

Method	Theory	ε_z	P = 0	P = 1	P = 2	P = 5	P = 10
L/h = 5, R/L = 5							
[11]	SNDT	= 0	0.8349	1.8836	2.6100	3.5873	4.0292
present	USDT	= 0	0.8766	1.9777	2.7405	3.7666	4.2306
L/h = 20, R/L = 5							
[11]	SNDT	= 0	0.5894	1.3754	1.8510	2.4409	2.7617
present	USDT	= 0	0.6188	1.4441	1.9435	2.5629	2.8997

Table 5: The dimensionless transverse deflection w values of CC 2DFGPCB with both uniform and uneven porosity, an aspect ratio of L/h = 5, and gradation exponents are considered.

P_x & P_z	L/h = 5	even porosity			P_x & P_z	L/h = 5	uneven porosity		
	0	0.1	0.2	0.3		0	0.1	0.2	0.3
0	0.4458	0.5111	0.5876	0.6782	0	0.4458	0.4641	0.4836	0.5043
1	1.4982	1.6419	1.8145	2.0189	1	1.4946	1.5826	1.6266	1.6727
2	2.1644	2.3686	2.6077	2.8910	2	2.2211	2.2783	2.3393	2.4040
5	3.1418	3.4224	3.7511	4.1404	5	3.1985	3.2771	3.3609	3.4499
10	3.5831	3.8982	4.2674	5.2046	10	3.6398	3.7281	3.8222	4.3221

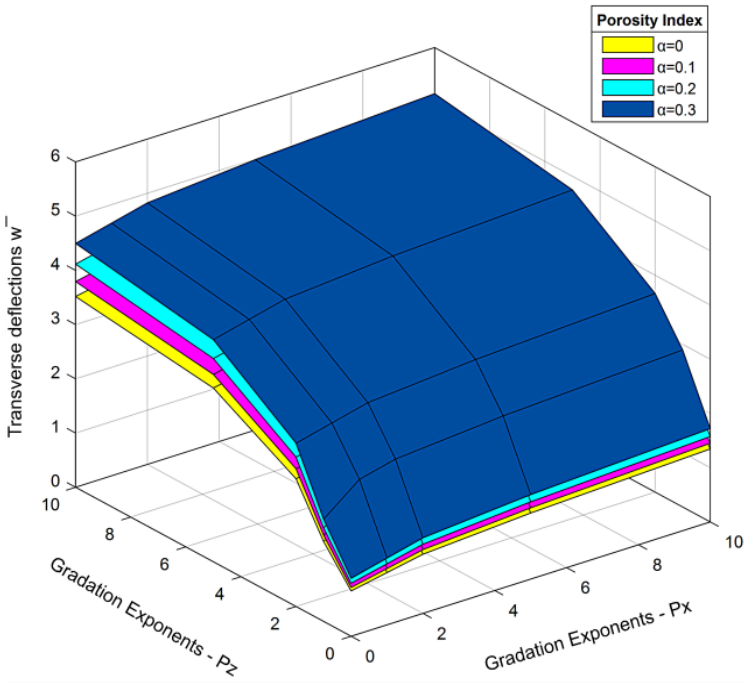

(a)

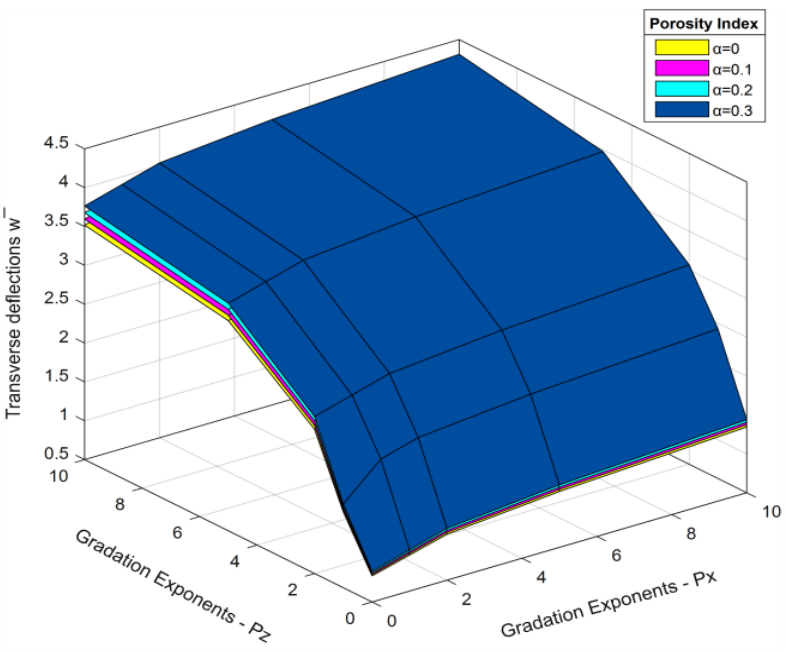

(b)

Fig 7: The dimensionless transverse deflections w values of CC 2DFGPCB with both (a) even and (b) uneven porosity, an aspect ratio of L/h = 5, and gradation exponents are provided

Table 6: Evaluation of dimensionless transverse deflection w values of CS 2DFGPCB using different theories for different aspect ratios (L/h = 5, L/h = 20) and gradation exponents

Method	Theory	ε_z	P = 0	P = 1	P = 2	P = 5	P = 10
L/h = 5, R/L = 5							
[11]	SNDT	= 0	1.4497	3.2536	4.4382	5.9811	6.5451
present	USDT	= 0	1.5221	3.4162	4.6601	6.2801	6.8723
L/h = 20, R/L = 5							
[11]	SNDT	= 0	1.2572	2.6612	3.6266	4.5933	5.6261
present	USDT	= 0	1.3200	2.7942	3.8079	4.8229	5.9074

Table 7: Dimensionless transverse deflections $\overline{w}$ values of CS 2DFGPCB with uneven and even porosity, aspect ratio (L/h = 5), and gradation exponents

P_x & P_z	L/h = 5	even porosity			P_x & P_z	L/h=5	uneven porosity		
	0	0.1	0.2	0.3		0	0.1	0.2	0.3
0	1.5221	1.9046	2.0374	2.1948	0	1.5221	1.8635	1.9438	2.0335
1	2.5962	2.8509	3.1491	3.5024	1	2.5962	2.7587	2.9389	3.1403
2	3.7803	4.1276	4.5343	5.0161	2	3.7803	4.0019	4.2477	4.5224
5	5.3233	5.7913	6.3394	6.9887	5	5.3233	5.6221	5.9534	6.3235
10	6.1657	6.6997	7.3249	8.6656	10	6.1659	6.5066	6.8846	7.9767

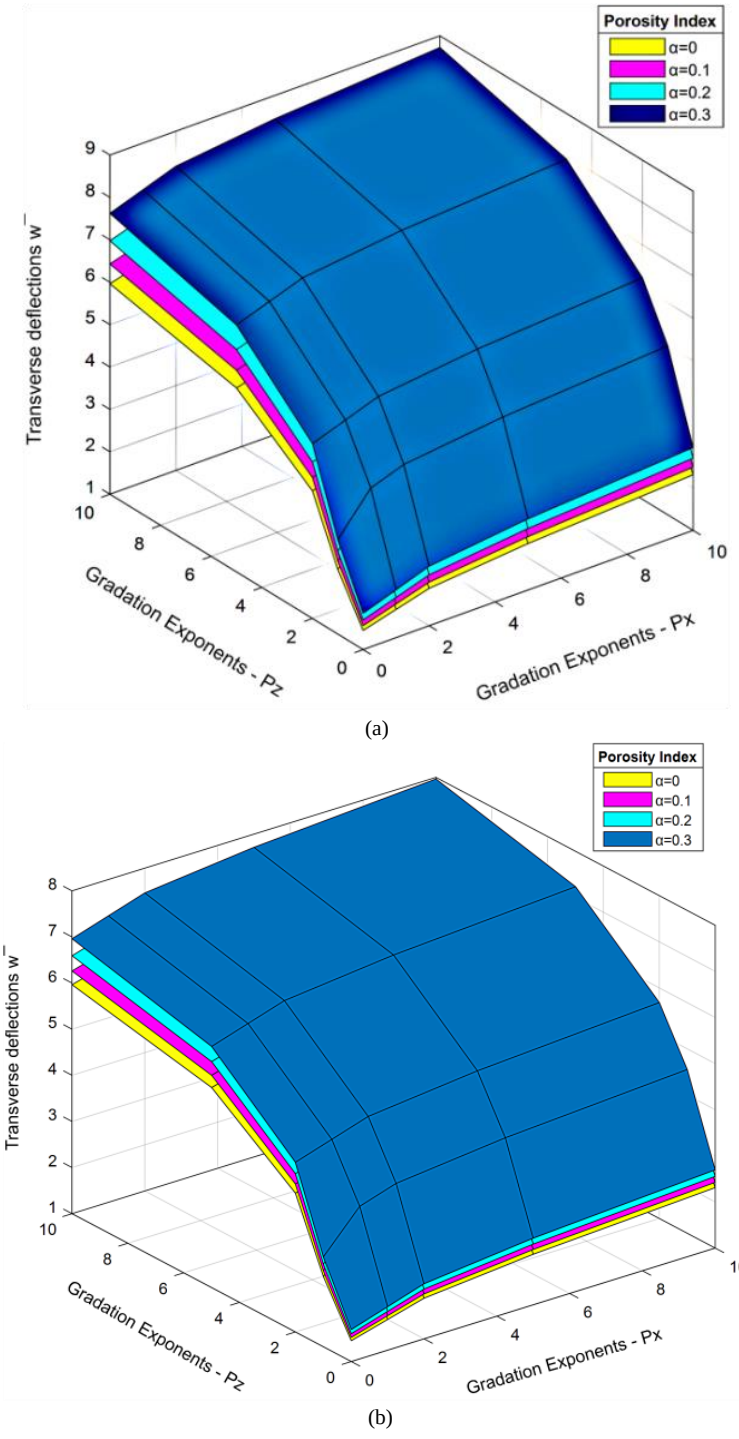

Fig 8: Dimensionless Transverse deflections $\overline{W}$ values of CS 2DFGPCB with (a) even (b) uneven porosity, aspect ratio (L/h = 5), and gradation exponents

Analyzed 2-directional FGCB with porous material under UDL at various conditions at the boundary (SS, CC and CS), aspect ratios (L/h = 5 & 20) and gradation exponents (p = 0, 1, 2, 5 and 10) and porosity coefficient (α = 0, 0.1, 0.2 and 0.3) for finding dimensionless transverse deflections. Numerical values of transverse deflection as shown in Tables 2, 4 and 6. The modulus of elasticity of a beam decreases as the value of its gradient exponents grows; hence the transverse deflection increases as the gradient exponents increase in the x and z directions. In other words, its dimensionless transverse deflection values increase larger as the value of the power law exponent increases. Because a change in the conditions of the boundary indicates a change in the stiffness of the beam, the values of the non-

dimensional maximum deflection for the SS FGM beam are larger than those for the remaining boundary conditions (CC and CS).

Table 2 shows the comparison of dimensionless transverse deflection for straight at L/h = 5 and 20; curved beams at R/L = 5 and 20 under SS boundary conditions. In straight beams i.e., under SSNDT, the $\bar{w}$ increases from 3.1397 to 10.8979 with an increase in the gradient index $P_x = 0$ to $P_x = 10$. Furthermore, with an increase in the aspect ratio, the $\bar{w}$ decreases for all values of gradient index. At L/h = 20, the $\bar{w}$ increases from 2.8947 to 9.5749 with an increase in the gradient index $P_x = 0$ to $P_x = 10$. On the other hand, for a curved beam under USDT, at R/L = 5, the $\bar{w}$ increases from 3.2966 to 11.4428 with an increase in the gradient index $P_x = 0$ to $P_x = 10$. Likewise, at R/L = 20, the $\bar{w}$ increases from 3.0394 to 10.0536 with an increase in the gradient index $P_x = 0$ to $P_x = 10$.

Table 4 shows the comparison of dimensionless transverse deflection for straight at L/h = 5 and 20; curved beams at R/L = 5 and 20 under CC boundary conditions. In straight beams i.e., under SSNDT, the $\bar{w}$ increases from 0.8349 to 4.0292 with an increase in the gradient index $P_x = 0$ to $P_x = 10$. Furthermore, with an increase in the aspect ratio, the $\bar{w}$ decreases for all values of gradient index. At L/h = 20, the $\bar{w}$ increases from 0.5894 to 2.7617 with an increase in the gradient index $P_x = 0$ to $P_x = 10$. On the other hand, for a curved beam under USDT, at R/L = 5, the $\bar{w}$ increases from 0.8766 to 4.2306 with an increase in the gradient index $P_x = 0$ to $P_x = 10$. Likewise, at R/L = 20, the $\bar{w}$ increases from 0.6188 to 2.8997 with an increase in the gradient index $P_x = 0$ to $P_x = 10$.

Table 6 shows the comparison of dimensionless transverse deflection for straight at L/h = 5 and 20; curved beams at R/L = 5 and 20 under CS boundary conditions. In straight beams i.e., under SSNDT, the $\bar{w}$ increases from 1.4497 to 6.5451 with an increase in the gradient index $P_x = 0$ to $P_x = 10$. Furthermore, with an increase in the aspect ratio, the $\bar{w}$ decreases for all values of gradient index. At L/h = 20, the $\bar{w}$ increases from 1.2572 to 5.6261 with an increase in the gradient index $P_x = 0$ to $P_x = 10$. On the other hand, for a curved beam under USDT, at R/L = 5, the $\bar{w}$ increases from 1.5221 to 6.8723 with an increase in the gradient index $P_x = 0$ to $P_x = 10$. Likewise, at R/L = 20, the $\bar{w}$ increases from 1.3200 to 5.9074 with an increase in the gradient index $P_x = 0$ to $P_x = 10$.

The decrease in dimensionless transverse deflections, which is explained by influence of length of the beam, i.e., aspect ratio increases means the length is increased, leads to decrease the dimensionless transverse deflections. It shows that as beams are scaled down in size, their bending stiffness improves since there is less material to bend. In general, curved beams have slightly higher values than straight beams for the same P_x values. This suggests that the distortion or the quantity being depicted is more noticeable in beams with a curved shape. The differences become more significant as P_x increases, suggesting that the grading effect is more pronounced in curved beams.

The SNDT typically considers both the shear deformation and the normal deformation in beams. This theory is particularly useful for analyzing straight beams, where the distribution of shear stress is assumed to be parabolic or linear along the thickness of the beam. The USDT is an advanced theoretical approach that aims to provide a more accurate representation of shear deformation in beams, especially curved beams. USDT incorporates higher-order shear deformation effects and a more realistic distribution of shear stress and strain across the beam's thickness, which is particularly important for thick and FGMs. For curved beams, USDT is particularly important because it captures the additional deformation due to curvature, which is not adequately represented by simpler theories. The persistent rise in values for curved beams under USDT, in contrast to straight beams, highlights the theory's capacity to accurately simulate the intricate behavior of curved structures.

Transverse deflection values as a function of porosity coefficient are tabulated in Tables 3, 5 and 7 . Since the flexural rigidity of the 2DFGPCB decreases with increasing porosity, transverse deflection increases in all boundary conditions as the porosity coefficient rises (Figs 6, 7 and 8). This effect is most pronounced for high values of porosities. The results indicate that the deflection of functionally graded circular beams is generally higher than that of functionally graded straight beams under identical loading conditions as shown in Table 2, 4 and 6. This difference is attributed to the additional bending moments and the shift in the neutral axis induced by the curvature of the circular beams. Furthermore, the influence of the gradation profile on the deflection is more pronounced in curved beams compared to straight beams due to the complex stress distribution resulting from the geometry.

The effective integration of USDT in the analysis of deflection in 2DFGPCB is advantageous that the shear deformation effects are more pronounced in the thick beams than in the slender beams. These effects are neglected in elementary theory of beam bending. In order to describe the correct bending behavior of thick beams including shear deformation effects and associated cross sectional warping, shear deformation theories are required. This can be accomplished by selection of proper kinematics and constitutive models.

4. Research implications

The implications of the analysis of deflection in a 2DFGPCB are that, the use of functionally graded porous materials can significantly reduce the weight of aerospace components, such as wings and fuselage parts, while maintaining or enhancing their mechanical properties. Understanding deflection behavior helps in optimizing the design for better performance under aerodynamic loads. Curved and straight beams with optimized material gradation

can be used in the design of components to manage vibrations and dynamic loads more effectively, improving the safety and longevity of aircraft. Bridges often utilize both straight and curved beams. Functionally graded materials can enhance the load-bearing capacity and durability of bridge components, leading to longer-lasting and safer structures. Reduced deflection under load can minimize maintenance costs and extend the service life of bridges. Lightweight and strong beams are crucial in the design of robotic arms and structures. The study's findings can help in creating more agile and capable robotic systems, particularly in industries like manufacturing and healthcare.

5. Conclusion

Functionally graded materials enhance the structural performance of beams by optimizing material properties, the curvature in circular beams introduces additional factors that significantly affect their deflection. These findings are crucial for the design and application of FG beams in engineering structures, particularly in fields where curved geometries are prevalent, such as aerospace, automotive, and civil engineering. Future research may involve the use of numerical methods, such as finite element analysis, to further validate the analytical results and explore the behavior under different loading and boundary conditions.

- Gradient exponents in x and z increase transverse deflection. Which is explained by material stiffness: increasing gradient exponents decreases beam modulus of elasticity.
- Mid-plane axial stress is zero, but it is clear that these values are not zero at the 2DFGPCB mid-plane for other values of gradient exponent. Due to the modulus of elasticity variation through the beam thickness, the neutral plane moves toward the top of the 2DFGPCB.
- Conditions at the boundary affect beam rigidity, the non-dimensional maximum deflection with SS 2DFGPCB is higher than with the other conditions at the boundary.
- By choosing appropriate gradient indexes, bending of 2DFGPCBs may be regulated to match the design requirements.
- In a curved beam, the neutral axis shifts towards the center of curvature, causing non-uniform stress distribution and affecting deflection.
- Curved beams experience additional bending moments due to the curvature, leading to higher stress concentrations on the inner side of the curve.
- The curvature term accounts for the increased deflection in the curved beam compared to straight beam.

References

[1] N. Hebbar, I. Hebbar, D. Ouinas, M. Bourada, Numerical modeling of bending, buckling, and vibration of functionally graded beams by using a higher-order shear deformation theory, *Frattura ed Integrità Strutturale,* Vol. 14, No. 52, pp. 230-246, 2020.

[2] A. RAZOUKI, B. Lhoucine, E. B. Khalid, The Exact Analytical Solution of the Bending Analysis of Thick Functionally Graded Beams with Higher Order Shear Deformation Theory Using Differential Transform Method, *International Journal of Advanced Research in Engineering and Technology (IJARET),* Vol. 11, No. 5, 2020.

[3] S. Coskun, J. Kim, H. Toutanji, Bending, free vibration, and buckling analysis of functionally graded porous micro-plates using a general third-order plate theory, *Journal of Composites Science,* Vol. 3, No. 1, pp. 15, 2019.

[4] R. Sayyad, V. Rathi, P. Kolase, Bending Analysis of Functionally Graded Beam Curved in Elevation Using Higher Order Theory, *International Research Journal of Engineering and Technology (IRJET),* Vol. 6, No. 8, pp. 361-367, 2019.

[5] J. Kim, K. K. Żur, J. N. Reddy, Bending, free vibration, and buckling of modified couples stress-based functionally graded porous micro-plates, *Composite Structures,* Vol. 209, pp. 879-888, 2019.

[6] M. Lezgy-Nazargah, A four-variable global–local shear deformation theory for the analysis of deep curved laminated composite beams, *Acta Mechanica,* Vol. 231, No. 4, pp. 1403-1434, 2020.

[7] H. Hu, T. Yu, T. Q. Bui, Dynamic and static isogeometric analysis for laminated Timoshenko curved microbeams, *Engineering Analysis with Boundary Elements,* Vol. 128, pp. 90-104, 2021.

[8] M. S. Beg, M. Y. Yasin, Bending, free and forced vibration of functionally graded deep curved beams in thermal environment using an efficient layerwise theory, *Mechanics of Materials,* Vol. 159, pp. 103919, 2021.

[9] M.-O. Belarbi, M. S. A. Houari, H. Hirane, A. A. Daikh, S. P. A. Bordas, On the finite element analysis of functionally graded sandwich curved beams via a new refined higher order shear deformation theory, *Composite Structures,* Vol. 279, pp. 114715, 2022.

[10] A. S. Sayyad, Y. M. Ghugal, A sinusoidal beam theory for functionally graded sandwich curved beams, *Composite Structures,* Vol. 226, pp. 111246, 2019.
[11] A. Karamanlı, Bending analysis of two directional functionally graded beams using a four-unknown shear and normal deformation theory, *Politeknik Dergisi,* Vol. 21, No. 4, pp. 861-874, 2018.
[12] A. S. Sayyad, P. V. Avhad, A new higher order shear and normal deformation theory for the free vibration analysis of sandwich curved beams, *Composite Structures,* Vol. 280, pp. 114948, 2022.
[13] Y. Pei, L. Li, Comment on the Navier's solution in "A sinusoidal beam theory for functionally graded sandwich curved beams"(Composite Structures 226 (2019) 111246), *Composite Structures,* Vol. 243, pp. 112248, 2020.
[14] L. Hadji, F. Bernard, N. Zouatnia, Bending and free vibration analysis of porous-functionally-graded (PFG) beams resting on elastic foundations, *Fluid Dynamic and Material Process,* Vol. 19, No. 4, pp. 1043-1054, 2023.
[15] M. Saad, L. Hadji, Thermal buckling analysis of porous FGM plates, *Materials Today: Proceedings,* Vol. 53, pp. 196-201, 2022.
[16] M. Avcar, L. Hadji, R. Akan, The influence of Winkler-Pasternak elastic foundations on the natural frequencies of imperfect functionally graded sandwich beams, *Geomechanics and Engineering,* Vol. 31, No. 1, pp. 99-112, 2022.
[17] L. Hadji, A. Fallah, M. M. Aghdam, Influence of the distribution pattern of porosity on the free vibration of functionally graded plates, *Structural Engineering and Mechanics,* Vol. 82, No. 2, pp. 151-161, 2022.
[18] R. Madan, S. Bhowmick, L. Hadji, A. Tounsi, Limit elastic speed analysis of rotating porous annulus functionally graded disks, *Steel and Composite Structures,* Vol. 42, No. 3, pp. 375-388, 2022.
[19] A. S. Sayyad, P. V. Avhad, L. Hadji, On the static deformation and frequency analysis of functionally graded porous circular beams, *Forces in Mechanics,* Vol. 7, pp. 100093, 2022.
[20] G. M. B. Chami, A. Kahil, L. Hadji, Influence of porosity on the fundamental natural frequencies of FG sandwich beams, *Materials Today: Proceedings,* Vol. 53, pp. 107-112, 2022.
[21] X. Wang, Z. Yuan, C. Jin, 3D free vibration analysis of multi-directional FGM parallelepipeds using the quadrature element method, *Applied mathematical modelling,* Vol. 68, pp. 383-404, 2019.
[22] H. Yang, C. Dong, Y. Wu, Postbuckling analysis of multi-directional perforated FGM plates using NURBS-based IGA and FCM, *Applied Mathematical Modelling,* Vol. 84, pp. 466-500, 2020.
[23] S. Thai, V. X. Nguyen, Q. X. Lieu, Bending and free vibration analyses of multi-directional functionally graded plates in thermal environment: A three-dimensional Isogeometric Analysis approach, *Composite Structures,* Vol. 295, pp. 115797, 2022.
[24] G. M. B. Chami, A. Kahil, L. Hadji, R. Madan, A. Tounsi, Free vibration analysis of multi-directional porous functionally graded sandwich plates, *Steel and Composite Structures, An International Journal,* Vol. 46, No. 2, pp. 263-277, 2023.
[25] L. Hadji, F. Bernard, R. Madan, A. Alnujaie, M. H. Ghazwani, Bending and buckling of porous multidirectional functionality graded sandwich plate, *Structural Engineering and Mechanics, An Int'l Journal,* Vol. 85, No. 2, pp. 233-246, 2023.
[26] Q.-H. Pham, V. K. Tran, P.-C. Nguyen, Hygro-thermal vibration of bidirectional functionally graded porous curved beams on variable elastic foundation using generalized finite element method, *Case Studies in Thermal Engineering,* Vol. 40, pp. 102478, 2022.
[27] I. Ahmadi, J. Sladek, V. Sladek, Size dependent free vibration analysis of 2D-functionally graded curved nanobeam by meshless method, *Mechanics of Advanced Materials and Structures,* pp. 1-22, 2023.
[28] A. Karamanli, T. P. Vo, Finite element model for free vibration analysis of curved zigzag nanobeams, *Composite Structures,* Vol. 282, pp. 115097, 2022.
[29] M. Motezaker, R. Kolahchi, D. K. Rajak, S. Mahmoud, Influences of fiber reinforced polymer layer on the dynamic deflection of concrete pipes containing nanoparticle subjected to earthquake load, *Polymer Composites,* Vol. 42, No. 8, pp. 4073-4081, 2021.
[30] M. Al-Furjan, M. H. Hajmohammad, X. Shen, D. K. Rajak, R. Kolahchi, Evaluation of tensile strength and elastic modulus of 7075-T6 aluminum alloy by adding SiC reinforcing particles using vortex casting method, *Journal of Alloys and Compounds,* Vol. 886, pp. 161261, 2021.
[31] R. Kolahchi, B. Keshtegar, N.-T. Trung, Optimization of dynamic properties for laminated multiphase nanocomposite sandwich conical shell in thermal and magnetic conditions, *Journal of Sandwich Structures & Materials,* Vol. 24, No. 1, pp. 643-662, 2022.
[32] P. Wan, M. Al-Furjan, R. Kolahchi, Nonlinear flutter response and reliability of supersonic smart hybrid nanocomposite rupture trapezoidal plates subjected to yawed flow using DQHFEM, *Aerospace Science and Technology,* Vol. 145, pp. 108862, 2024.

[33] C. Chu, M. Al-Furjan, R. Kolahchi, Energy harvesting and dynamic response of SMA nano conical panels with nanocomposite piezoelectric patch under moving load, *Engineering Structures*, Vol. 292, pp. 116538, 2023.

[34] M. Al-Furjan, S. Fan, L. Shan, A. Farrokhian, X. Shen, R. Kolahchi, Wave propagation analysis of micro air vehicle wings with honeycomb core covered by porous FGM and nanocomposite magnetostrictive layers, *Waves in Random and Complex Media*, pp. 1-30, 2023.

[35] M. Al-Furjan, R. Kolahchi, L. Shan, M. Hajmohammad, A. Farrokhian, X. Shen, Slamming impact induced hydrodynamic response in wave-piercing catamaran beam elements with controller, *Ocean Engineering*, Vol. 266, pp. 112908, 2022.

[36] M. Al-Furjan, M. Xu, A. Farrokhian, G. S. Jafari, X. Shen, R. Kolahchi, On wave propagation in piezoelectric-auxetic honeycomb-2D-FGM micro-sandwich beams based on modified couple stress and refined zigzag theories, *Waves in Random and Complex Media*, pp. 1-25, 2022.

[37] M. Al-Furjan, Y. Yang, A. Farrokhian, X. Shen, R. Kolahchi, D. K. Rajak, Dynamic instability of nanocomposite piezoelectric-leptadenia pyrotechnica rheological elastomer-porous functionally graded materials micro viscoelastic beams at various strain gradient higher-order theories, *Polymer Composites*, Vol. 43, No. 1, pp. 282-298, 2022.

[38] M. Al-Furjan, C. Yin, X. Shen, R. Kolahchi, M. S. Zarei, M. Hajmohammad, Energy absorption and vibration of smart auxetic FG porous curved conical panels resting on the frictional viscoelastic torsional substrate, *Mechanical Systems and Signal Processing*, Vol. 178, pp. 109269, 2022.

[39] P. Wan, M. Al-Furjan, R. Kolahchi, L. Shan, Application of DQHFEM for free and forced vibration, energy absorption, and post-buckling analysis of a hybrid nanocomposite viscoelastic rhombic plate assuming CNTs' waviness and agglomeration, *Mechanical Systems and Signal Processing*, Vol. 189, pp. 110064, 2023.